Title

Advances in the simulation of space-charge effects

Journal

Journal of Instrumentation, 15(07)

ISSN

1748-0221

Author

Qiang, J

Publication Date

2020-07-01

DOI

10.1088/1748-0221/15/07/P07028

Peer reviewed

PREPARED FOR SUBMISSION TO JINST

Advances in the simulation of space-charge effects

Ji Qiang,

Lawrence Berkeley National Laboratory
Berkeley, CA 94720, USA

E-mail: jqiang@lbl.gov

ABSTRACT: The nonlinear space-charge effects are an important topic in high intensity accelerator beam dynamics and have been extensively studied using macroparticle tracking simulations. In this paper, we report on recent advances in the simulation of space-charge effects using a symplectic multiparticle space-charge model. The transverse space-charge limit was explored for a periodic focusing and defocusing lattice. The artificial numerical emittance growth in the macroparticle space-charge simulation was analyzed using a one-dimensional model.

KEYWORDS: Beam dynamics, Accelerator modelling and simulations (multi-particle dynamics)

[1]Corresponding author.

Contents

1 Introduction

The nonlinear space-charge effects play an important role in high intensity/high brightness accelerators by causing beam emittance growth, halo formation, and particle loss. In the accelerator beam dynamics community, the space-charge effects were widely studied using a self-consistent particle-in-cell (PIC) method [1–10]. The numerical integrators in those space-charge models are generally not symplectic. A symplectic integrator is important in long-term classical dynamics simulation in order to preserve phase space structures [11, 12]. Recently, self-consistent symplectic space-charge models were proposed [13, 14]. In the following sections, we give an overview of the symplectic space-charge particle-in-cell model and apply this model to exploring transverse space-charge limits in a periodic focusing and defocusing accelerator lattice. We also analyze the numerical noise/fluctuation associated with the macroparticle deposition using a shape function in the PIC model. Such a fluctuation in the charge density results in space-charge force fluctuation and artificial numerical emittance growth in the space-charge simulation [15–18].

2 Symplectic self-consistent space-charge tracking model

For a multi-particle system with N_p charged particles subject to both space-charge self fields and external fields in an accelerator, an approximate Hamiltonian of the system can be derived from the single particle Hamiltonian [19, 20] as:

$$H = \sum_{i=1}^{N_p} \mathbf{p}_i^2/2 + \frac{1}{2}\sum_{i=1}^{N_p}\sum_{j=1}^{N_p} q\bar{\varphi}(\mathbf{r}_i, \mathbf{r}_j) + \sum_{i=1}^{N_p} q\psi(\mathbf{r}_i) \tag{2.1}$$

where $H(\mathbf{r}_1, \mathbf{r}_2, \cdots, \mathbf{r}_{N_p}, \mathbf{p}_1, \mathbf{p}_2, \cdots, \mathbf{p}_{N_p}; s)$ denotes the Hamiltonian of the system using distance s as an independent variable, $\bar{\varphi}$ is the space-charge interaction potential (including both the direct electric potential and the longitudinal vector potential) between the charged particles i and j, ψ denotes the potential associated with the external field, $\mathbf{r}_i = (x_i, y_i, \theta_i = \omega\Delta t)$ denotes the normalized canonical spatial coordinates of particle i, $\mathbf{p}_i = (p_{xi}, p_{yi}, p_{ti} = -\Delta E/mc^2)$ the normalized

canonical momentum coordinates of particle i, and ω the reference angular frequency, Δt the time of flight to location s, ΔE the energy deviation with respect to the reference particle, m the rest mass of the particle, and c the speed of light in vacuum. The equations governing the motion of individual particle i follow the Hamilton's equations as:

$$\frac{d\mathbf{r}_i}{ds} = \frac{\partial H}{\partial \mathbf{p}_i} \tag{2.2}$$

$$\frac{d\mathbf{p}_i}{ds} = -\frac{\partial H}{\partial \mathbf{r}_i} \tag{2.3}$$

Let ζ denote a 6N-vector of coordinates, the above Hamilton's equation can be rewritten as:

$$\frac{d\zeta}{ds} = -[H, \zeta] \tag{2.4}$$

where [,] denotes the Poisson bracket. A formal solution for the above equation after a single step τ can be written as:

$$\zeta(\tau) = \exp(-\tau(: H :))\zeta(0) \tag{2.5}$$

Here, we have defined a differential operator $: H :$ as $: H : g = [H,\ g]$, for arbitrary function g. For a Hamiltonian that can be written as a sum of two terms $H = H_1 + H_2$, an approximate solution to above formal solution can be written as [21]:

$$\begin{aligned}\zeta(\tau) &= \exp(-\tau(: H_1 : + : H_2 :))\zeta(0) \\ &= \exp(-\frac{1}{2}\tau : H_1 :) \exp(-\tau : H_2 :) \exp(-\frac{1}{2}\tau : H_1 :)\zeta(0) + O(\tau^3)\end{aligned} \tag{2.6}$$

Let $\exp(-\frac{1}{2}\tau : H_1 :)$ define a transfer map $\mathcal{M}_1$ and $\exp(-\tau : H_2 :)$ a transfer map $\mathcal{M}_2$, for a single step, the above splitting results in a second order numerical integrator for the original Hamilton's equation as:

$$\begin{aligned}\zeta(\tau) &= \mathcal{M}(\tau)\zeta(0) \\ &= \mathcal{M}_1(\tau/2)\mathcal{M}_2(\tau)\mathcal{M}_1(\tau/2)\zeta(0) + O(\tau^3)\end{aligned} \tag{2.7}$$

The above numerical integrator can be extended to 4^{th} order accuracy and arbitrary even-order accuracy following Yoshida's approach [22]. This numerical integrator Eq. 2.7 will be symplectic if both the transfer map $\mathcal{M}_1$ and the transfer map $\mathcal{M}_2$ are symplectic. A transfer map $\mathcal{M}_i$ is symplectic if and only if the Jacobian matrix M_i of the transfer map $\mathcal{M}_i$ satisfies the following condition:

$$M_i^T J M_i = J \tag{2.8}$$

where J denotes the $6N \times 6N$ matrix given by:

$$J = \begin{pmatrix} 0 & I \\ -I & 0 \end{pmatrix} \tag{2.9}$$

and I is the $3N \times 3N$ identity matrix.

For the Hamiltonian in Eq. 2.1, we can choose H_1 as:

$$H_1 = \sum_{i=1}^{N_p} \mathbf{p}_i^2/2 + \sum_{i=1}^{N_p} q\psi(\mathbf{r}_i) \tag{2.10}$$

This corresponds to the Hamiltonian of a group of charged particles subject to external fields. The symplectic transfer map $\mathcal{M}_1$ for this Hamiltonian can be obtained for most accelerator beam line elements using a Lie algebra method [23].

The H_2 can be written as:

$$H_2 = \frac{1}{2} \sum_{i=1}^{N_p} \sum_{j=1}^{N_p} q\bar{\varphi}(\mathbf{r}_i, \mathbf{r}_j) \tag{2.11}$$

which includes the space-charge effects and is only a function of position. For the space-charge Hamiltonian $H_2(\mathbf{r})$, the single step transfer map $\mathcal{M}_2$ can be written as:

$$\mathbf{r}_i(\tau) = \mathbf{r}_i(0) \tag{2.12}$$

$$\mathbf{p}_i(\tau) = \mathbf{p}_i(0) - \frac{\partial H_2(\mathbf{r})}{\partial \mathbf{r}_i}\tau \tag{2.13}$$

The Jacobi matrix of the above transfer map $\mathcal{M}_2$ is

$$M_2 = \begin{pmatrix} I & 0 \\ L & I \end{pmatrix} \tag{2.14}$$

where L is a $3N \times 3N$ matrix. For the M_2, in order to satisfy the symplectic condition Eq. 2.8, the matrix L needs to be a symmetric matrix, i.e.

$$L = L^T \tag{2.15}$$

Given the fact that $L_{ij} = \partial \mathbf{p}_i(\tau)/\partial \mathbf{r}_j = -\frac{\partial^2 H_2(\mathbf{r})}{\partial \mathbf{r}_i \partial \mathbf{r}_j}\tau$, the matrix L will be symmetric as long as it is *analytically calculated* from the function H_2. If both the transfer map $\mathcal{M}_1$ and the transfer map $\mathcal{M}_2$ are symplectic, the numerical integrator Eq. 2.7 for multi-particle tracking will be symplectic.

For a coasting beam, the multi-particle Hamiltonian H_2 can be obtained from the single particle Hamiltonian [19] as:

$$H_2 = \frac{K}{2} \sum_{i=1}^{N_p} \sum_{j=1}^{N_p} \varphi(\mathbf{r}_i, \mathbf{r}_j) \tag{2.16}$$

where $K = qI/(2\pi\epsilon_0 p_0 v_0^2 \gamma_0^2)$ is the generalized perveance, I is the beam current, ϵ_0 is the permittivity of vacuum, p_0 is the momentum of the reference particle, v_0 is the speed of the reference particle, γ_0 is the relativistic factor of the reference particle, and φ is the space charge Coulomb interaction potential. In this Hamiltonian, the effects of the direct Coulomb electric potential and the longitudinal vector potential are combined together. The electric Coulomb potential φ in the Hamiltonian H_2 can be obtained from the solution of the Poisson equation. In the following, we

assume that the coasting beam is inside a rectangular perfectly conducting pipe. In this case, the two-dimensional Poisson's equation can be written as:

$$\frac{\partial^2\phi}{\partial x^2} + \frac{\partial^2\phi}{\partial y^2} = -4\pi\rho \tag{2.17}$$

where ϕ is the electric potential, and ρ is the particle density distribution of the beam.

The boundary conditions for the electric potential inside the rectangular perfectly conducting pipe are:

$$\phi(x = 0, y) = 0 \tag{2.18}$$
$$\phi(x = a, y) = 0 \tag{2.19}$$
$$\phi(x, y = 0) = 0 \tag{2.20}$$
$$\phi(x, y = b) = 0 \tag{2.21}$$

where a is the horizontal width of the pipe and b is the vertical width of the pipe.

Given the boundary conditions in Eqs. 2.18-2.21, the electric potential ϕ and the source term ρ can be approximated using two sine functions as [24–26]:

$$\rho(x, y) = \sum_{l=1}^{N_l}\sum_{m=1}^{N_m} \rho^{lm} \sin(\alpha_l x)\sin(\beta_m y) \tag{2.22}$$
$$\phi(x, y) = \sum_{l=1}^{N_l}\sum_{m=1}^{N_m} \phi^{lm} \sin(\alpha_l x)\sin(\beta_m y) \tag{2.23}$$

where

$$\rho^{lm} = \frac{4}{ab}\int_0^a\int_0^b \rho(x, y)\sin(\alpha_l x)\sin(\beta_m y)\, dxdy \tag{2.24}$$
$$\phi^{lm} = \frac{4}{ab}\int_0^a\int_0^b \phi(x, y)\sin(\alpha_l x)\sin(\beta_m y)\, dxdy \tag{2.25}$$

where $\alpha_l = l\pi/a$ and $\beta_m = m\pi/b$. The above approximation follows the numerical spectral Galerkin method since each basis functions satisfies the boundary conditions on the wall [24]. For a smooth function, this spectral approximation has an accuracy whose numerical error scales as $O(\exp(-cN))$ with $c > 0$, where N is the number of the basis function (i.e. mode number in each dimension) used in the approximation. By substituting above expansions into the Poisson Eq. 2.17 and making use of the orthonormal condition of the sine functions, we obtain

$$\phi^{lm} = \frac{4\pi\rho^{lm}}{\gamma_{lm}^2} \tag{2.26}$$

where $\gamma_{lm}^2 = \alpha_l^2 + \beta_m^2$.

In the simulation, the particle density distribution function $\rho(x, y)$ can be represented as:

$$\rho(x, y) = \frac{1}{\Delta x\Delta y N_p}\sum_{j=1}^{N_p} S(x - x_j)S(y - y_j) \tag{2.27}$$

where $S(x)$ is a unitless shape function (i.e. deposition function in the PIC model) Δx and Δy are mesh cell size in each dimension. The use of the shape function helps smooth the density function when the number of macroparticles in the simulation is much less than the real number of particles in the beam. Using the above equation and Eq. 2.24 and Eq. 2.26, we obtain:

$$\phi^{lm} = \frac{4\pi}{\gamma_{lm}^2}\frac{4}{ab}\frac{1}{N_p}\sum_{j=1}^{N_p}\frac{1}{\Delta x\Delta y}\int_0^a\int_0^b S(x-x_j)S(y-y_j)\sin(\alpha_l x)\sin(\beta_m y)dxdy \quad (2.28)$$

and the electric potential as:

$$\phi(x,y) = 4\pi\frac{4}{ab}\frac{1}{N_p}\sum_{j=1}^{N_p}\sum_{l=1}^{N_l}\sum_{m=1}^{N_m}\frac{1}{\gamma_{lm}^2}\sin(\alpha_l x)\sin(\beta_m y)$$
$$\frac{1}{\Delta x\Delta y}\int_0^a\int_0^b S(\bar{x}-x_j)S(\bar{y}-y_j)\sin(\alpha_l\bar{x})\sin(\beta_m\bar{y})d\bar{x}d\bar{y} \quad (2.29)$$

From the above electric potential, the interaction potential φ between particles i and j can be written as:

$$\varphi(x_i,y_i,x_j,y_j) = 4\pi\frac{4}{ab}\frac{1}{N_p}\sum_{l=1}^{N_l}\sum_{m=1}^{N_m}\frac{1}{\gamma_{lm}^2}\frac{1}{\Delta x\Delta y}\int_0^a\int_0^b S(x-x_j)S(y-y_j)\sin(\alpha_l x)\sin(\beta_m y)dxdy$$
$$\frac{1}{\Delta x\Delta y}\int_0^a\int_0^b S(x-x_i)S(y-y_i)\sin(\alpha_l x)\sin(\beta_m y)dxdy \quad (2.30)$$

where the interpolation function to the particle location is assumed to be the same as the deposition function. Now, the space-charge Hamiltonian H_2 can be written as:

$$H_2 = 4\pi\frac{K}{2}\frac{4}{ab}\frac{1}{N_p}\sum_{i=1}^{N_p}\sum_{j=1}^{N_p}\sum_{l=1}^{N_l}\sum_{m=1}^{N_m}\frac{1}{\gamma_{lm}^2}$$
$$\frac{1}{\Delta x\Delta y}\int_0^a\int_0^b S(x-x_j)S(y-y_j)\sin(\alpha_l x)\sin(\beta_m y)dxdy$$
$$\frac{1}{\Delta x\Delta y}\int_0^a\int_0^b S(x-x_i)S(y-y_i)\sin(\alpha_l x)\sin(\beta_m y)dxdy \quad (2.31)$$

If the deposition shape function is assumed to be a Dirac delta function, and the particle distribution function $\rho(x,y)$ can be represented as:

$$\rho(x,y) = \frac{1}{N_p}\sum_{j=1}^{N_p}\delta(x-x_j)\delta(y-y_j) \quad (2.32)$$

The space-charge Hamiltonian H_2 can be written as:

$$H_2 = 4\pi\frac{K}{2}\frac{4}{ab}\frac{1}{N_p}\sum_{i=1}^{N_p}\sum_{j=1}^{N_p}\sum_{l=1}^{N_l}\sum_{m=1}^{N_m}\frac{1}{\gamma_{lm}^2}\sin(\alpha_l x_j)\sin(\beta_m y_j)\sin(\alpha_l x_i)\sin(\beta_m y_i) \quad (2.33)$$

The one-step symplectic transfer map $\mathcal{M}_2$ of the particle i with this Hamiltonian is given as:

$$p_{xi}(\tau) = p_{xi}(0) - \tau 4\pi K \frac{4}{ab}\frac{1}{N_p}\sum_{j=1}^{N_p}\sum_{l=1}^{N_l}\sum_{m=1}^{N_m}\frac{\alpha_l}{\gamma_{lm}^2}\sin(\alpha_l x_j)\sin(\beta_m y_j)\cos(\alpha_l x_i)\sin(\beta_m y_i)$$
$$p_{yi}(\tau) = p_{yi}(0) - \tau 4\pi K \frac{4}{ab}\frac{1}{N_p}\sum_{j=1}^{N_p}\sum_{l=1}^{N_l}\sum_{m=1}^{N_m}\frac{\beta_m}{\gamma_{lm}^2}\sin(\alpha_l x_j)\sin(\beta_m y_j)\sin(\alpha_l x_i)\cos(\beta_m y_i) \tag{2.34}$$

where both p_{xi} and p_{yi} are normalized by the reference particle momentum p_0.

If the shape function is not a delta function, the one-step symplectic transfer map $\mathcal{M}_2$ of the particle i with this space-charge Hamiltonian H_2 is given as:

$$\begin{aligned}
p_{xi}(\tau) = p_{xi}(0) &- \tau 4\pi K \frac{4}{ab}\frac{1}{N_p}\sum_{j=1}^{N_p}\sum_{l=1}^{N_l}\sum_{m=1}^{N_m}\frac{1}{\gamma_{lm}^2}\frac{1}{\Delta x\Delta y}\int_0^a\int_0^b S(x-x_j)S(y-y_j)\sin(\alpha_l x)\sin(\beta_m y)dxdy \\
&\frac{1}{\Delta x\Delta y}\int_0^a\int_0^b \frac{\partial S(x-x_i)}{\partial x_i}S(y-y_i)\sin(\alpha_l x)\sin(\beta_m y)dxdy \\
p_{yi}(\tau) = p_{yi}(0) &- \tau 4\pi K \frac{4}{ab}\frac{1}{N_p}\sum_{j=1}^{N_p}\sum_{l=1}^{N_l}\sum_{m=1}^{N_m}\frac{1}{\gamma_{lm}^2}\frac{1}{\Delta x\Delta y}\int_0^a\int_0^b S(x-x_j)S(y-y_j)\sin(\alpha_l x)\sin(\beta_m y)dxdy \\
&\frac{1}{\Delta x\Delta y}\int_0^a\int_0^b S(x-x_i)\frac{\partial S(y-y_i)}{\partial y_i}\sin(\alpha_l x)\sin(\beta_m y)dxdy
\end{aligned} \tag{2.35}$$

Assuming that the shape function is a compact local function with respect to the computational grid, after approximating the integral with a summation on the grid, the above map can be rewritten as:

$$\begin{aligned}
p_{xi}(\tau) &= p_{xi}(0) - \tau 4\pi K \sum_I\sum_J \frac{\partial S(x_I - x_i)}{\partial x_i}S(y_J - y_i)\phi(x_I, y_J) \\
p_{yi}(\tau) &= p_{yi}(0) - \tau 4\pi K \sum_I\sum_J S(x_I - x_i)\frac{\partial S(y_J - y_i)}{\partial y_i}\phi(x_I, y_J)
\end{aligned} \tag{2.36}$$

where

$$\phi(x_I, y_J) = \frac{4}{ab}\sum_{l=1}^{N_l}\sum_{m=1}^{N_m}\frac{1}{\gamma_{lm}^2}\sum_{I'}\sum_{J'}\bar{\rho}(x_{I'}, y_{J'})\sin(\alpha_l x_{I'})\sin(\beta_m y_{J'})\sin(\alpha_l x_I)\sin(\beta_m y_J) \tag{2.37}$$

and

$$\bar{\rho}(x_{I'}, y_{J'}) = \frac{1}{N_p}\sum_{j=1}^{N_p} S(x_{I'} - x_j)S(y_{J'} - y_j), \tag{2.38}$$

where the integers I, J, I', and J' denote the two dimensional computational grid index, and the summations with respect to those indices are limited to the range of a few local grid points depending on the specific deposition function.

In the PIC literature, several compact shape functions are used in the simulation. For example, a quadratic shape function is given as [27, 28]:

$$S(x_I - x_i) = \begin{cases} \frac{3}{4} - (\frac{x_i - x_I}{\Delta x})^2, & |x_i - x_I| \le \Delta x/2 \\ \frac{1}{2}(\frac{3}{2} - \frac{|x_i - x_I|}{\Delta x})^2, & \Delta x/2 < |x_i - x_I| \\ & \le 3/2\Delta x \\ 0 & \text{otherwise} \end{cases} \tag{2.39}$$

The derivative of the above quadratic shape function is:

$$\frac{\partial S(x_I - x_i)}{\partial x_i} = \begin{cases} -2(\frac{x_i - x_I}{\Delta x})/\Delta x, & |x_i - x_I| \le \Delta x/2 \\ (-\frac{3}{2} + \frac{(x_i - x_I)}{\Delta x})/\Delta x, & \Delta x/2 < |x_i - x_I| \le 3/2\Delta x, \quad x_i > x_I \\ (\frac{3}{2} + \frac{(x_i - x_I)}{\Delta x})/\Delta x, & \Delta x/2 < |x_i - x_I| \le 3/2\Delta x, \quad x_i \le x_I \\ 0 & \text{otherwise} \end{cases} \tag{2.40}$$

The same shape function and its derivative can be applied to the y dimension.

Using the symplectic transfer map $\mathcal{M}_1$ for the external field Hamiltonian H_1 from a magnetic optics code and the transfer map $\mathcal{M}_2$ for the space-charge Hamiltonian H_2, one obtains a symplectic PIC model including the self-consistent space-charge effects.

3 An application example

The above self-consistent multi-particle tracking model was applied to study space-charge effects in a linear periodic quadrupole focusing and defocusing (FODO) lattice. In this example, a one GeV proton coasting beam subject to space-charge effects is transported through the lattice inside a perfectly conducting square pipe with an aperture size of 10 mm. It was tracked through twenty thousand lattice periods using the above self-consistent symplectic particle-in-cell model with a quadratic shape function. A schematic plot of the lattice is shown in Fig. 1. It consists of a 0.1

Figure 1. Schematic plot of a FODO lattice [14].

m focusing quadrupole magnet and a 0.1 m defocusing quadrupole magnet within a single period. The total length of the period is 1 meter. The zero current phase advance through one lattice period is about 85 degrees. Such a lattice with zero current phase advance below 90 degrees avoids the envelope instability in the accelerator design. The proton beam has an initial transverse normalized emittance of 1 μm and a 4D Gaussian distribution in phase space. Given the periodic lattice and the initial rms matched Gaussian distribution, we scanned the beam current from 100 A to 550 A. This corresponds to a depressed phase advance from 72 degrees to 37 degrees. Varying the beam current helps determine the limit of space-charge effects in this type of accelerator lattice and identify potential instabilities that cause beam emittance blow up. Figure 2 shows the four dimensional emittance growth $(\frac{\epsilon_x}{\epsilon_{x0}}\frac{\epsilon_y}{\epsilon_{y0}} - 1)\%$ at the end of 20,000 lattice periods as a function of depressed phase advance. For the large depressed phase advance above 45 degrees (i.e. small beam

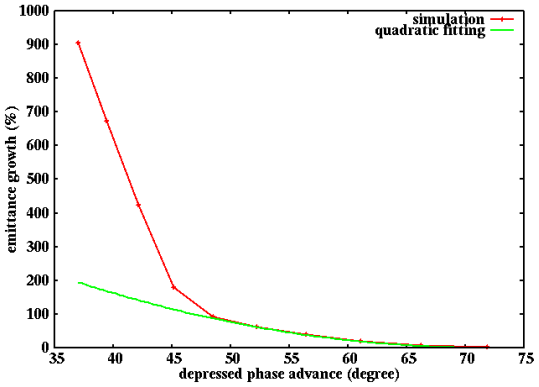

Figure 2. Four dimensional emittance growth as a function of depressed phase advance from the multi-particle simulation (purple) and from a quadratic fitting (green).

current), there is small emittance growth through the accelerator lattice. Such an emittance growth is mainly caused by the numerical noise associated with the finite number of macroparticles used in the simulation. Here, we have used about $100,000$ macroparticles with 257×257 grid points and 32×32 cutoff modes. The numerical noise driven emittance growth scales quadratically with respect to the beam current and will be discussed in the following section. For the small depressed phase advance (large beam current), the final emittance growth is significantly greater than that from the numerical noise.

Figure 3 shows the horizontal emittance evolution through $20,000$ lattice periods with 42.1 degree phase advance and 48.5 degree phase advance. It is seen that for the 42.1 degree phase advance case, the emittance starts to grow exponentially after five thousand lattice periods. This might be caused by the space-charge driven collective instability [29]. The slow emittance growth in the 48.5 degree phase advance case is due to numerical noise effects.

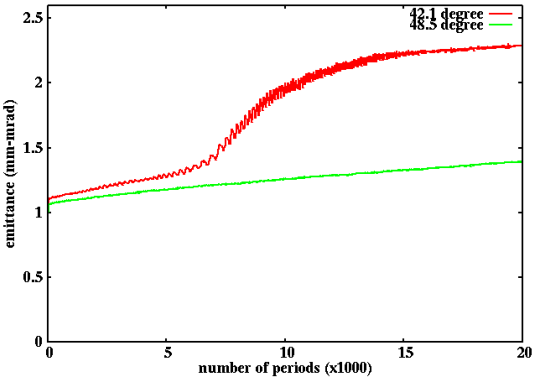

Figure 3. Four dimensional emittance growth evolution from the multi-particle simulation with 42.1 degree depressed phase advance (yellow) and with 48.5 degree depressed phase advance (green).

4 Numerical Emittance Growth in Space-Charge Simulations

The use of finite number of macroparticles in the above multi-particle tracking simulation causes numerical noise in the charge density distribution and space-charge fields. This results in artificial emittance growth in the simulation, even with the use of the self-consistent symplectic space-charge model. This is seen in the above example with 48.5 degree phase advance (Fig. 3) in the absence of major instabilities. This numerical artifact can be understood using the following one-dimensional model.

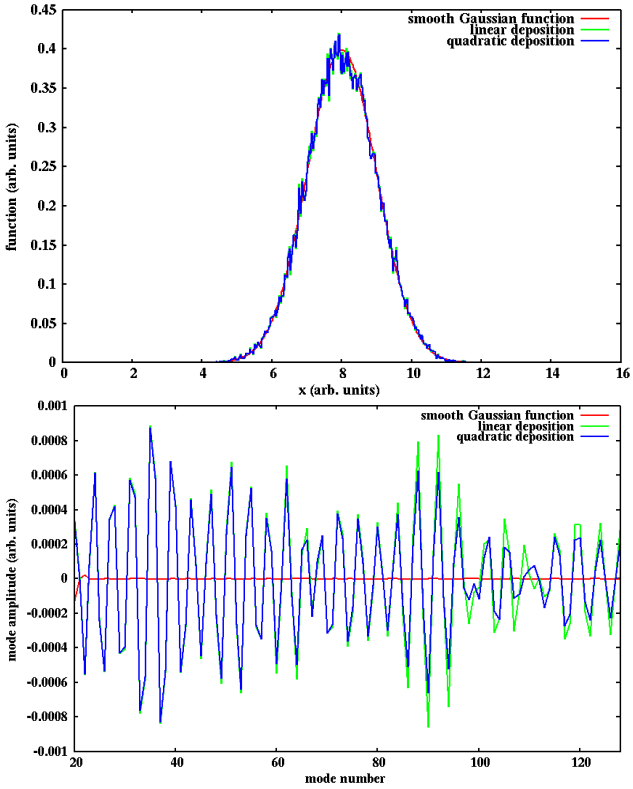

Figure 4. A Gaussian function (top) and its spectral mode amplitude (bottom) as a function of mode number from the smooth Gaussian function on the grid (red), from the linear particle deposition (green) and the quadratic particle deposition (blue) on the grid using 25, 000 macroparticles and 128 grid cells.

Following the spectral method used in the above symplectic PIC model, the solution of space-charge electric potential ϕ^l in the frequency domain can be obtained from the solution of the one-dimensional Poisson equation as:

$$\phi^l = \frac{Q\rho^l}{\epsilon_0 \alpha_l^2} \tag{4.1}$$

where Q is the charge of the beam, ρ^l is the density distribution function in the frequency domain, $\alpha_l = l\pi/L$, L is the length of the domain, and l is the mode number in frequency domain. Using the above sine function expansion, the amplitude of density mode l from the sampled macroparticle

deposition can be obtained as:

$$\rho^l = \frac{1}{N_p}\frac{2}{L}\sum_{i=1}^{N_p}\sum_{I=1}^{N_g} S(x_I - x_i)\sin(\alpha_l x_I) \tag{4.2}$$

where N_p is the total number of macroparticles and N_g is the total number of grid cells.

To illustrate the numerical noise associated with macroparticles, we use a one-dimensional Gaussian distribution function $\exp(-(x-4)^2/2)/\sqrt{2\pi}$ as an example, sample it with a number of macroparticles, and reconstruct the function on a grid using a shape function. Figure 4 shows the smooth Gaussian function, the reconstructed Gaussian functions, and the mode amplitude as a function of mode number from the smooth Gaussian function on the grid, from the linear particle deposition, and from the quadratic particle deposition on the grid using 25, 000 macroparticles and 128 grid cells. It is seen that for the smooth Gaussian distribution function, with mode number beyond 20, the mode amplitude is nearly zero while the mode amplitude from the macroparticle deposition fluctuates with a magnitude of about 10^{-4}. Those nonzero amplitude modes contribute to the fluctuation in density distribution and induce artificial numerical emittance growth. The mode fluctuation amplitude becomes smaller from the linear deposition to the quadratic deposition shape function. The quadratic shape function spreads a macroparitcle across three grid points and results in less high frequency density fluctuation than the linear shape function that spreads a macroparticle across two grid points.

The fluctuation of each density mode from the macroparticle deposition can be estimated quantitatively using standard deviation (or variance) of the mode amplitude. Given the density mode amplitude ρ^l in Eq. 4.2, the variance of ρ^l can be calculated as:

$$var(\rho^l) = \frac{1}{N_p}(\frac{2}{L})^2 var(\sum_{I=1}^{N_g} S(x_I - x_i)\sin(\alpha_l x_I)) \tag{4.3}$$

where

$$\begin{aligned} var(\sum_{I} S(x_I - x_i)\sin(\alpha_l x_I)) \approx\ & (\frac{1}{N_p}\sum_{i=1}^{N_p}[\sum_{I=1}^{N_g} S(x_I - x_i)\sin(\alpha_l x_I)]^2) - \\ & (\frac{1}{N_p}\sum_{i=1}^{N_p}[\sum_{I=1}^{N_g} S(x_I - x_i)\sin(\alpha_l x_I)])^2 \end{aligned} \tag{4.4}$$

Here, we assume that the particle coordinate x_i is independently sampled from a probability density distribution function $\rho(x)$.

If the shape function is a delta function, the variance of the density mode l can be obtained as:

$$var(\sum_{I=1}^{N_g} S(x_I - x_i)\sin(\alpha_l x_I)) = var(\sin(\alpha_l x)) \tag{4.5}$$

where

$$var(\sin(\alpha_l x)) = \int_0^L \sin^2(\alpha_l x)\rho(x)dx - (\int_0^L \sin(\alpha_l x)\rho(x)dx)^2 \tag{4.6}$$

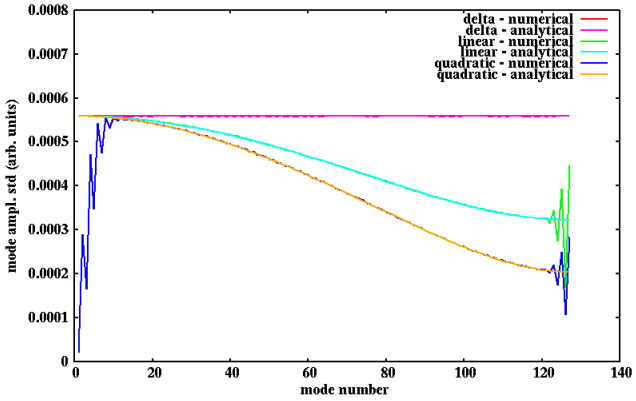

Figure 5. Mode amplitude standard deviation as a function of mode number from the delta shape function (red), the linear particle shape function (green), and the quadratic particle shape function (blue) on the grid using 25, 000 macroparticles and 128 grid cells. The analytical estimates for large mode number are also plotted here for the delta shape function (magenta), the linear function (light blue), and the quadratic function (orange).

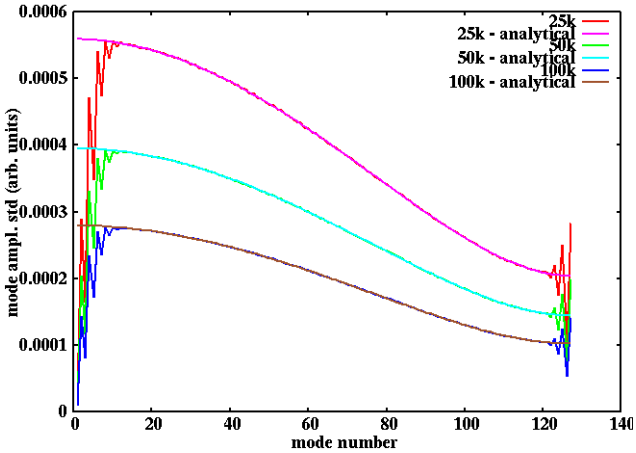

Figure 6. Mode amplitude standard deviation as a function of mode number from the quadratic particle deposition shape function using 25, 000 (red), 50, 000 (green) and 100, 000 (blue) macroparticles and 128 grid cells and from the analytical estimates for large mode number.

For a large mode number l, $var(\sin(\alpha_l x)) \approx 1/2$, and $var(\rho^l) \approx \frac{1}{2}(\frac{2}{L})^2 \frac{1}{N_p}$.

If the shape function is a compact linear function, the variance of the density mode l can be obtained as:

$$var(\sum_{I=1}^{N_g} S(x_I - x_i)\sin(\alpha_l x_I)) \approx var(\sin(\alpha_l x)) + \frac{1}{3}(\cos(\alpha_l \Delta) - 1)\int \sin^2(\alpha_l x)\rho(x)dx + \frac{1}{6}\sin(\alpha_l \Delta)\int \sin(2\alpha_l x)\rho(x)dx \quad (4.7)$$

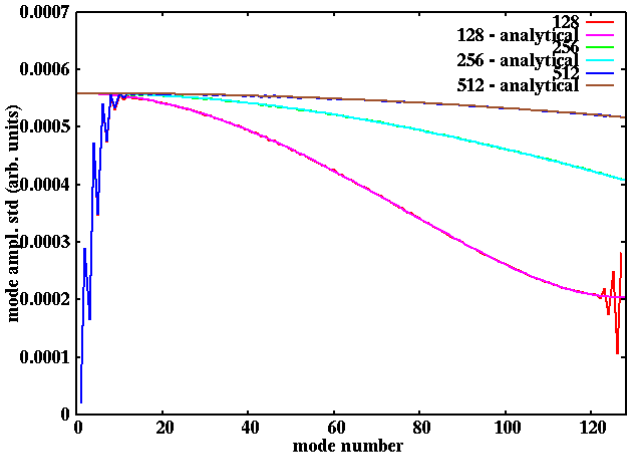

Figure 7. Mode amplitude standard deviation as a function of mode number from the quadratic particle deposition shape function using 25,000 and 128, 256 and 512 grid cells and from the analytical estimates for large mode number.

For a large mode number l, the variance can be approximated as:

$$var(\sum_{I=1}^{N_g} S(x_I - x_i)\sin(\alpha_l x_I)) \approx var(\sin(\alpha_l x)) + \frac{1}{6}(\cos(\alpha_l \Delta) - 1) \tag{4.8}$$

and

$$var(\rho^l) \approx (\frac{2}{L})^2 \frac{1}{N_p}(\frac{2}{6} + \frac{1}{6}\cos(\alpha_l \Delta)) \tag{4.9}$$

where $\Delta = L/N_g$ is the grid cell size inside the computational domain. As the grid cell size goes to zero, the variance of the mode amplitude from the linear deposition shape function approaches that from the delta shape function. For a finite size grid cell, the variance of the mode amplitude from the linear function is less than that from the delta shape function. This variance becomes smaller with larger grid cell size and for larger mode number. The use of finite size grid cell with linear deposition shape function helps smooth out high frequency density fluctuation in the macroparticle simulation.

If the shape function is a quadratic function as shown in Eq. 2.39, the variance of the density mode l can be obtained as:

$$\begin{aligned} var(\sum_{I=1}^{N_g} S(x_I - x_i)\sin(\alpha_l x_I)) \approx\ & var(\sin(\alpha_l x)) + \\ & [\frac{26}{60}(\cos(\alpha_l \Delta) - 1) + \frac{1}{60}(\cos(2\alpha_l \Delta) - 1)] \int \sin^2(\alpha_l x)\rho(x)dx \\ & + [\frac{26}{120}\sin(\alpha_l \Delta) + \frac{1}{120}\sin(2\alpha_l \Delta)] \int \sin(2\alpha_l x)\rho(x)dx \end{aligned} \tag{4.10}$$

For a large mode number l, the variance can be approximated as:

$$var(\sum_{I=1}^{N_g} S(x_I - x_i)\sin(\alpha_l x_I)) \approx var(\sin(\alpha_l x)) + [\frac{26}{120}(\cos(\alpha_l\Delta) - 1) + \frac{1}{120}(\cos(2\alpha_l\Delta) - 1)] \tag{4.11}$$

and

$$var(\rho^l) \approx (\frac{2}{L})^2 \frac{1}{N_p}(\frac{33}{120} + \frac{26}{120}\cos(\alpha_l\Delta) + \frac{1}{120}\cos(2\alpha_l\Delta)) \tag{4.12}$$

When the grid cell goes to zero, the variance of the density mode amplitude from the quadratic shape function also approaches that from the delta shape function. For a finite grid cell size, the variance of the mode amplitude is further reduced in comparison to that from the linear shape function. The compact quadratic shape function has a larger spread than the compact linear shape function and provides further smoothing to the high frequency density fluctuation.

From the variance of each mode amplitude, one can calculate the standard deviation (std) of each mode amplitude by taking the square root of the variance. Figure 5 shows the mode amplitude standard deviation as a function of mode number for the above Gaussian function by using the delta shape function, the linear deposition shape function, and the quadratic deposition shape function from both the numerical calculation using Eq. 4.4 and the above analytical estimates for large mode numbers. It is seen that the analytical estimates agree with the numerical calculations very well for large mode numbers. The mode amplitude standard deviation is small at small mode number and increases quickly to 10^{-4} level and start to decrease after about 10 modes for the linear and the quadratic shape functions. For small mode numbers, all three shape functions yield about the same amplitude fluctuation standard deviations. For large mode numbers (high frequencies), both the linear shape function and the quadratic shape function give smaller model amplitude standard deviation than the delta shape function. The quadratic deposition shape function gives the least fluctuation standard deviation for large mode numbers, and is most effective to smooth out high frequency noise among the three shape functions.

In Fig. 6, we show the mode amplitude standard deviation as a function of mode number from the using 25, 000, 50, 000, and 100, 000 macroparticle sampling of the Gaussian distribution and from the analytical estimates for large mode numbers using the quadratic shape function. The standard deviation decreases with the increase of the macroparticle number and scales as $1/\sqrt{N_p}$ as expected from the Eq. 4.3. The analytical estimates agree very well with the numerical calculations for those three macroparticle samplings.

Figure 7 shows the mode amplitude standard deviation as a function of mode number from the using 128, 256, and 512 grid cells and 25, 000 macroparticles for the above Gaussian distribution and from the analytical estimates using the quadratic shape function. The analytical estimates show good agreement with the numerical calculations for large mode numbers in all three grid cells. For small mode numbers (less than 10), the standard deviation is close among three grid cells. This is because $\alpha_l\Delta$ is small in this regime and the standard deviation from the quadratic shape function approaches that from the delta shape function, which is independent of grid cell size. For larger mode numbers, the term containing $\alpha_l\Delta$ becomes important as seen in Eq. 4.12. The standard

deviation with smaller number of grid cells (i.e. larger cell size) becomes smaller due to the cosine function dependence on the cell size.

The fluctuation in the density mode amplitude results in fluctuation in the solution of space-charge forces. From the density mode amplitude variance, we obtain the variance of space-charge electric potential mode amplitude from the solution of Poisson's equation as:

$$var(\phi^l) = \frac{Q^2}{\epsilon_0^2 \alpha_l^4} var(\rho^l) \tag{4.13}$$

This might be used to estimate fluctuation amplitude of the space-charge forces. The effect of random fluctuation force on beam emittance growth can be calculated following the approximate solution to the stochastic differential equation [30]. After one step τ, the new coordinates (in one-dimension) can be approximated as:

$$x_2 = x_1 \tag{4.14}$$

$$x_2' = x_1' + \delta F \sqrt{\tau} \tag{4.15}$$

where δF denotes the random fluctuation force. The new emittance under the effect of this force will be:

$$\begin{aligned} \epsilon_2^2 &= < x_2^2 >< x_2'^2 > - < x_2 x_2' >^2 \\ &= \epsilon_1^2 + 2(< x_1^2 >< x_1' \delta F > - < x_1 x_1' >< x_1 \delta F >)\sqrt{\tau} \\ &\quad +(< x_1^2 >< \delta F^2 > - < x_1 \delta F >^2)\tau \end{aligned} \tag{4.16}$$

where <> denotes the average with respect to the particle distribution. Using the assumption that δF is a random fluctuation and independent of x and x', i.e. $< x\delta F >= 0$, and $< x'\delta F >= 0$, we obtain:

$$\epsilon_2^2 = \epsilon_1^2 + < x_1^2 >< \delta F^2 > \tau \tag{4.17}$$

The emittance growth will be:

$$\Delta\epsilon \approx \frac{1}{2}(< x^2 >< (\delta F)^2 > \tau/\epsilon, \tag{4.18}$$

and the emittance growth rate will be:

$$\frac{\Delta\epsilon/\epsilon}{\tau} \approx \frac{1}{2}\frac{< x^2 >< (\delta F)^2 >}{\epsilon^2} \tag{4.19}$$

This emittance growth rate due to the random force error is independent of time step size and is proportional to the variance of the random force error that is inversely proportional to the number of macroparticles used in the simulation and is proportional to the square of the beam bunch intensity. This quadratic dependence on bunch intensity is seen in Fig. 2 of the preceding application simulations. The dependence on the number of macroparticles can be seen in Fig. 8 that shows the 4D emittance growth rate as a function of macroparticle number in the linear FODO lattice using 256×256 grid cells [18]. It is seen that the emittance growth rate scales as $1/N_p$, which agrees well with the scaling of the random sample fluctuation induced emittance growth.

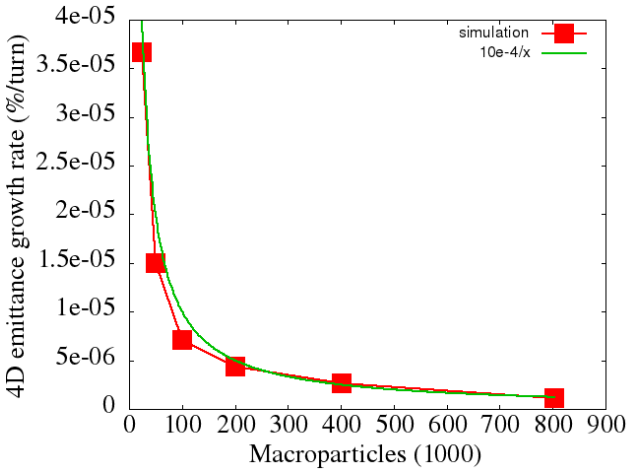

Figure 8. The 4D emittance growth rate as a function of the simulation macroparticle number using the FODO lattice [18].

5 Conclusions

In this paper, we reviewed a recently developed symplectic multi-particle tracking model and applied this model to the study of transverse space-charge limits in a periodic focusing and defocusing channel. The simulation results show the appearance of space-charge driven collective instability when the depressed phase advance is below 45 degrees or the corresponding tune depression below about 0.5. A further study is on going to understand the underlying mechanism of the instability.

We also observed numerical emittance growth in a stable parameter setting due to the macroparticle sampling noise. This numerical noise driven emittance growth was studied using a one-dimensional model. We calculated the fluctuation amplitude of particle density modes (and hence space-charge potential modes) from the deposition of the macroparticle sampled Gaussian function. The analytical solutions agree with the numerical results very well and clearly show the smoothing effects from finite size grid cell on high frequency sampling noise. The larger cell size causes smaller density mode fluctuation amplitude. For the same cell size, the second order quadratic deposition shape function yields smaller fluctuation amplitude than the linear shape function. The variance of the charge density mode fluctuation scales inversely with the number of macroparticles and is proportional to the square of beam bunch intensity. This results in artificial numerical emittance growth rate inversely proportional to the number of macroparticles used in the space-charge simulation and proportional to the square of bunch intensity.

Acknowledgments

This work was supported by the U.S. Department of Energy under Contract No. DE-AC02-05CH11231, and used computer resources at the National Energy Research Scientific Computing Center.

References

[1] A. Friedman, D. P. Grote, and I. Haber, *Three-Dimensional Particle Simulations of Heavy Ion Fusion Beams*, *Phys. Fluids B* **4**, (1992) p. 2203.

[2] H. Takeda and J. H. Billen, *Recent developments of the accelerator design code PARMILA*, in Proc. XIX International Linac Conference, Chicago, August 1998, p. 156.

[3] J. Qiang, R. D. Ryne, S. Habib, V. Decyk, *An object-oriented parallel particle-in-cell code for beam dynamics simulation in linear accelerators J. Comput. Phys.* **163**, (2000) p. 434.

[4] R. Duperrier, *TOUTATIS: A radio frequency quadrupole code*, *Phys. Rev. ST Accel. Beams* **3**, (2000) 124201.

[5] J. D. Galambos, S. Danilov, D. Jeon, J. A. Holmes, and D. K. Olsen, F. Neri and M. Plum, *Comparison of simulated and observed beam profile broadening in the Proton Storage Ring and the role of space charge*, *Phys. Rev. ST Accel. Beams* **3**, (2000) 034201.

[6] P. N. Ostroumov and K. W. Shepard, *Correction of beam-steering effects in low-velocity superconducting quarter-wave cavities*, *Phys. Rev. ST. Accel. Beams* **11**, (2001) 110101.

[7] J. Qiang, S. Lidia, R. D. Ryne, and C. Limborg-Deprey, *A three-dimensional quasi-static model for high brightnees beam dynamics simulation*, *Phys. Rev. ST Accel. Beams* **9**, (2006) 044204.

[8] J. Amundson, P. Spentzouris, J. Qiang and R. Ryne, *Synergia, an accelerator modeling tool with 3-D space charge*, *J. Comp. Phys.* **211**, (2006) 229.

[9] opal code homepage at PSI, https://gitlab.psi.ch/OPAL.

[10] J. Qiang, R. D. Ryne, M. Venturini, A. A. Zholents, and I. V. Pogorelov, *High resolution simulation of beam dynamics in electron linacs for x-ray free electron lasers*, *Phys. Rev. ST Accel. Beams* **12**, (2009) 100702.

[11] P. J. Channell and C. Scovel, *Symplectic integration of Hamiltonian systems*, *Nonlinearity* **3**, (1990) p.231.

[12] T. J. Stuchi, *Symplectic Integrators Revisited*, *Brazilian J. Phys.* **32**, p. 958 (2002).

[13] J. Qiang, *Symplectic multiparticle tracking model for self-consistent space-charge simulation*, *Phys. Rev. Accel. Beams* **20**, (2017) 014203.

[14] J. Qiang, *Symplectic particle-in-cell model for space-charge beam dynamics simulation*, *Phys. Rev. Accel. Beams* **21**, (2018) 054201.

[15] J. Struckmeier, *Concept of entropy in the realm of charged particle beams*, *Phys. Rev. E* **54**, (1996) 830.

[16] I. Hofmann and O. Boine-Frankenheim, *Grid dependent noise and entropy growth in anisotropic 3d particle-in-cell simulation of high intensity beams*, *Phys. Rev. ST Accel. Beams* **17**, (2014) 124201.

[17] F. Kesting and G. Franchetti, *Propagation of numerical noise in particle-in-cell tracking*, *Phys. Rev. ST Accel. Beams* **18**, (2015) 114201.

[18] J. Qiang, *Long-term simulation of space-charge effects*, *Nuclear Inst. and Methods in Physics Research* **A918**, (2019) p. 1.

[19] R. D. Ryne, *Computational Methods in Accelerator Physics*, US Particle Accelerator class note, 2012.

[20] G. Fubiani, J. Qiang, E. Esarey, and W. P. Leemans, *Space charge modeling of dense electron beams with large energy spreads*, *Phys. Rev. ST Accel. Beams* **9**, (2006) 064402.

[21] E. Forest and R. D. Ruth, *Fourth-order symplectic integration*, *Physica D* **43**, (1990) p. 105.

[22] H. Yoshida, *Construction of higher order symplectic integrators*, *Phys. Lett. A* **150**, (1990) p. 262.

[23] A. J. Dragt, *Lie Methods for Nonlinear Dynamics with Applications to Accelerator Physics*, 2016.

[24] D. Gottlieb and S. A. Orszag, *Numerical Analysis of Spectral Methods: Theory and Applications*, Society for Industrial and Applied Mathematics, 1977.

[25] J. Qiang and R. D. Ryne, *Parallel 3D Poisson solver for a charged beam in a conducting pipe*, *Comput. Phys. Commun.* **138**, (2001) p. 18.

[26] J. Qiang, *Efficient three-dimensional Poisson solvers in open rectangular conducting pipe*, *Comput. Phys. Commun.* **203**, (2016) p. 122.

[27] R.W. Hockney, J.W. Eastwood, *Computer Simulation Using Particles*, Adam Hilger, New York, 1988.

[28] C. K. Birdsall and A. B. Langdon, *Plasma Physics via Computer Simulation*, (CRC Press, New York, 2004), p. 174.

[29] I. Hofmann, L. J. Laslett, L. Smith, and I. Haber, *Stability of the Kapchinskij-Vladimirskij (KV) distribution in long periodic transport systems*, *Part. Accel.* **13**, (1983) p. 145.

[30] J. Qiang, *Emittance growth due to random force error*, *Nuclear Inst. and Methods in Physics Research* **A948**, (2019) 162844.